20th AIAA Computational Fluid Dynamics Conference
27 - 30 June 2011, Honolulu, Hawaii

AIAA 2011-3851

High Order Accurate Finite-Difference Methods: as seen in OVERFLOW

Thomas H. Pulliam *

NASA Ames Research Center
MS T27B, Moffett Field, CA 94035

Conventional finite-difference methods are the main workhorse of NASA's OVERFLOW code. Recent enhancements in the development, implementation and analysis of simple high-order accurate finite-difference techniques within OVERFLOW are documented here. Results are presented for simple vortex propagation to demonstrate the salient features of the methods, and more complex three-dimensional rotorcraft flows are used to validate their usefulness in real applications.

I. Introduction

The focus in this paper is on the development of high order accurate finite-difference operators as implemented in OVERFLOW,[1] a three-dimensional, Reynolds-averaged Navier-Stokes code using an overset approach for large scale, complicated geometry applications. Implementation issues associated with larger difference stencil widths, parallelization, overset strategies, implicit time integration and effects on accuracy, stability and convergence will be discussed. Periodic vortex propagation is used to demonstrate the salient features of the methods, and a complex application for an isolated rotor in hover will be presented showing improvements in accuracy and efficiency for practical problems.

II. Approach and Results

II.A. Equations

The two-dimensional Euler equations on a Cartesian grid (no assumption is made as to the orientation of axes, so some generality is maintained) are used as the starting point for the development and to establish notation. The extension to the three-dimensional general curvilinear coordinate form of the Navier-Stokes equations, while not completely straightforward, is consistent with the development presented here.

The two-dimensional Euler equations on a Cartesian grid are

$$\partial_t Q + \partial_x E + \partial_y F = 0 \tag{1}$$

so that, $\mathcal{F}(Q) = \partial_x E + \partial_y F$ with

$$Q = \begin{bmatrix} \rho \\ \rho u \\ \rho v \\ e \end{bmatrix}, \quad E = \begin{bmatrix} \rho u \\ \rho u^2 + p \\ \rho u v \\ u(e+p) \end{bmatrix}, \quad F = \begin{bmatrix} \rho v \\ \rho u v \\ \rho v^2 + p \\ v(e+p) \end{bmatrix} \tag{2}$$

with Q the conservative variables, density ρ, x-momentum ρu, y-momomtum ρv and energy e, pressure $p = (\gamma - 1)(e - 0.5\rho(u^2 + v^2))$ and $\gamma = 1.4$ for a perfect gas,

*Senior Research Scientist, Associate Fellow AIAA

II.B. Test Case

An isolated vortex propagation problem is used as the test case. A two-dimensional (2D) uniform grid is assumed, with periodic boundary conditions in x and simple Dirichlet conditions in y enforced on a rectangular domain. The domain size for the results shown below is 10×10 units where the vortex core size (diameter) C_d is defined as 1.0 unit. The equations for the initial condition are a finite core vortex embedded in a free stream flow $Q_\infty = (\rho_\infty, M_\infty, 0, e_\infty)$ with $\rho_\infty = 1.0, M_\infty = 0.5, p_\infty = \frac{1}{\gamma}$, and $T_\infty = 1.0$. The perturbed (by the vortex) field is

$$\begin{aligned} T &= T_\infty - \frac{V_s^2(\gamma-1)}{16 G_s \gamma \pi^2} e^{2G_s(1-r^2)} \\ \rho &= T^{\frac{1}{(\gamma-1)}} \\ u &= M_\infty - \frac{V_s}{2\pi}(y-y_0) e^{G_s(1-r^2)} \\ v &= \frac{V_s}{2\pi}(x-x_0) e^{G_s(1-r^2)} \end{aligned} \tag{3}$$

with the vortex strength $V_s = 5.0$ and the Gaussian width scale $G_s = 0.5$. The vortex is initially centered at $x_0 = 5.0$ and $y_0 = 5.0$ and $r = \sqrt{(x-x_0)^2 + (y-y_0)^2}$. Figure 1 shows density contours of the initial vortex, which has a period of 10 C_d and unless stated all computed results are after 30 C_d or three revolutions of the vortex across the domain.

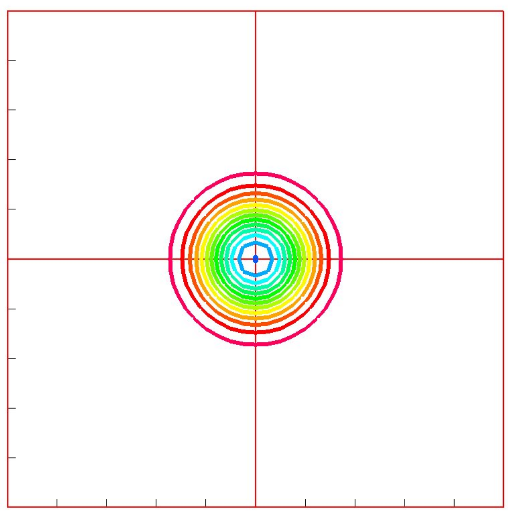

Figure 1. Density Contours, Initial Vortex

II.C. OVERFLOW: Overset Concepts

OVERFLOW[1] is a three-dimensional time-marching implicit Navier-Stokes code that can also operate in two-dimensional or axisymmetric mode. The code uses structured overset grid systems. Several different inviscid flux algorithms and implicit solution algorithms are included in OVERFLOW. The code has options for thin layer or full viscous terms. A wide variety of boundary conditions are also provided in the code. The code may also be used for multi-species and variable specific heat applications. Algebraic, one-equation, and two-equation turbulence models are available. Low speed preconditioning is also available for several of the inviscid flux algorithms and solution algorithms in the code. The code also supports bodies in relative motion, and includes both a six-degree-of-freedom (6-DOF) model and a grid assembly code. Collision detection and modeling is also included in OVERFLOW. The code is written to allow use of both MPI and OpenMP for parallel computing applications. OVERFLOW has two basic operational modes. The code can still *be run in the original OVERFLOW mode, which requires that all grids be supplied and assembled using PEGASUS[2] prior to the start of the solution process. The other option is OVERFLOW-D[3,4] mode which requires additional input files and inputs to control the Domain Connectivity Framework (DCF)[4,5] grid assembly, off-body grid generation, and 6-DOF or specified motion simulation. Only the near-body grids need to be supplied in OVERFLOW-D mode since Cartesian outer grids are automatically generated prior to grid assembly using DCF.* [b]

References[7–10] contain details of the various options, methods and features of the code. The development presented here is consistent with recent work by Nichols, Tramel and Buning[11] on high order WENO schemes. The discussion here, will be restricted to generic features of the overset process which are affected by the choices of difference operators and artificial dissipation schemes.

A few definitions are taken from the OVERFLOW manual.[6] In the setting of a finite-difference approach to spatial derivatives and the overset approach used in OVERFLOW, grid points can be classified as

- Field points: points on which the differential equations will be solved.
- Blanked-out points: points inside bodies or holes, where the solution is not computed or is ignored.
- Fringe points: inter-grid boundary points where solution values are obtained via interpolation from another grid. Single-fringe points have only one layer of interpolation points at a boundary. Double-fringe points have two layers of interpolated points at a boundary, triple have three, etc. Double-fringe points are the default in the code and allow 2^{nd} and 3^{rd} order flux algorithms to maintain their full five-point stencil across interpolated boundaries. The 5^{th} order schemes require a triple-fringe to maintain their seven-point stencil at interpolated boundaries. Reducing the number of fringe layers will result in the flux algorithm losing accuracy at interpolated boundaries.
- Donor points: points contributing to interpolation stencils providing interpolated data to fringe points.
- Orphan points: fringe points without valid donors, resulting from hole cutting failure (no possible donor) or only poor quality donors being available (insufficient overlap). In OVERFLOW, solution values at orphan points are set by averaging values from neighbors in the computational grid.

The particular focus here is on the fringe point requirements. As the stencil width of a particular finite-difference operator increases, the number of required fringe points increases. For example, let j be the grid point index, a five point stencil finite-difference operator using points $(j-2, j-1, j, j+1, j+2)$ applied at an overset boundary on the left at $j = 3$ would by definition have $(j = 3, 4, 5, \dots)$ as field points and $(j = 1, 2)$ as fringe points. If the difference stencil is expanded to seven points, then an additional left fringe point is required. In general, the hole cutting and interpolation are automatically handled by the OVERFLOW process, but the requirement on fringe points needs to be satisfied based on the required stencil size for the chosen operators. In the subsequent development, fringe point requirements will defined.

III. Difference Operators

Second order finite differences and third order artificial dissipation is the default approach employed in OVERFLOW, as defined below. Let j, k be the index counters for the x and y directions, respectively. Then $Q_{j,k}$ represents a single grid point value of Q. The difference equation is now

$$\partial_t Q_{j,k} + \delta_x E_{j,k} + \delta_y F_{j,k} = 0 \tag{4}$$

where δ_x and δ_y represent finite difference operators. Results were obtained with 40 grids points in both directions, unless otherwise specified.

III.A. Central Flux Differences

The basic central finite difference operator for the inviscid flux terms are defined below. The fluxes E, F are formed and differenced to 2^{nd} order as, e.g. in x

$$\partial_x E \approx {\delta_x}^{c2} E_{j,k} = \frac{E_{j+1,k} - E_{j-1,k}}{2\Delta x} \tag{5}$$

[b] Taken directly from the OVERFLOW Manual[6]

where $c2$ designates a 2^{nd} order central difference operator. Flux differences to 2^{nd} order require 1 fringe point.

A fourth order accurate option uses (the k part of the indices's is dropped for brevity)

$$\partial_x E \approx \delta_x^{c4} E_j = \frac{-E_{j+2} + 8E_{j+1} - 8E_{j-1} + E_{j-2}}{12\Delta x} \tag{6}$$

Flux differences to 4^{th} order require 2 fringe points.

A sixth order accurate option uses

$$\partial_x E \approx \delta_x^{c6} E_j = \frac{E_{j+3} - 9E_{j+2} + 45E_{j+1} - 45E_{j-1} + 9E_{j-2} - E_{j-3}}{60\Delta x} \tag{7}$$

Flux differences to 6^{th} order require 3 fringe points.

III.B. Artificial Dissipation

Numerical computations require some form of artificial dissipation, whether it is added explicitly to a central difference of the inviscid fluxes or implicitly by using an upwind operator scheme.

The standard method used in OVERFLOW is a mixed 2^{nd} and 4^{th} derivative artificial dissipation employing a pressure gradient switch and spectral radius scaling.[12] Expanding the definition of the artificial dissipation to include a higher order term which will result in a less dissipative operator and allow for up to a 5^{th} order scheme.

The artificial dissipation term is

$$\nabla_x (\sigma_{j+1} + \sigma_j) \left(\epsilon_j^{(2)} \Delta_x Q_j - \epsilon_j^{(4)} \Delta_x \nabla_x \Delta_x Q_j + \epsilon_j^{(6)} \Delta_x \nabla_x \Delta_x \nabla_x \Delta_x Q_j \right) / \Delta x \tag{8}$$

with

$$\nabla_x Q_j = (Q_j - Q_{j-1}), \quad \Delta_x Q_j = (Q_{j+1} - Q_j) \tag{9}$$

$$\begin{aligned} \epsilon_j^{(2)} &= \epsilon_2 \max(\Upsilon_{j+1}, \Upsilon_j, \Upsilon_{j-1}) && (10) \\ \Upsilon_j &= |p_{j+1} - 2p_j + p_{j-1}| / |p_{j+1} + 2p_j + p_{j-1}| \\ \epsilon_j^{(4,6)} &= \max(0, \max(\epsilon_4, \epsilon_6) - \epsilon_j^{(2)}) && (11) \end{aligned}$$

Similar terms are used in the y direction. The term σ_j is a spectral radius scaling and is defined as $\sigma_j = |u_j + a_j|$ with $a = \sqrt{\gamma p/\rho}$, the speed of sound.

Before discussing the suggested values of ϵ in Eq. 8, the implication of the various terms is examined. Letting $\sigma_{j+1} + \sigma_j = 1.0$, the term with coefficient $\epsilon_j^{(2)}$ is controlled by both the constant ϵ_2 and the gradient of pressure which is a switch to turn on 1^{st} order dissipation at discontinuities, e.g. shocks. Letting $\epsilon_4 = \epsilon_6 = 0$, $\Upsilon_j = 1.0$ and $\epsilon_j^{(2)} = \epsilon =$ constant, Eq. 8 becomes

$$\frac{\epsilon}{\Delta x} \nabla_x \Delta_x Q_j = \frac{\epsilon}{\Delta x} (Q_{j+1} - 2Q_j + Q_{j-1}) \equiv \epsilon(\Delta x) \partial_{xx} Q_j$$

a 1^{st} order term. This term would require one single fringe point.

Examining the effect of the second term in Eq. 8 by letting $\epsilon_2 = \epsilon_6 = 0$ and $\epsilon_j^{(4)} = \epsilon =$ constant,

$$\frac{\epsilon}{\Delta x} \nabla_x \Delta_x \nabla_x \Delta_x Q_j = \frac{\epsilon}{\Delta x} (Q_{j+2} - 4Q_{j+1} + 6Q_j - 4Q_{j-1} + Q_{j-2}) \equiv \epsilon(\Delta x)^3 \partial_{xxxx} Q_j$$

The artificial dissipation defined by this term in Eq. 8 is a 3^{rd} order term and represents a 4^{th} derivative dissipative operator and would require two fringe points for implementation.

Finally, the third term in Eq. 8, letting $\epsilon_2 = \epsilon_4 = 0$ and $\epsilon_j^{(6)} = \epsilon =$ constant, leads to

$$\begin{aligned} &\frac{\epsilon}{\Delta x} \nabla_x \Delta_x \nabla_x \Delta_x \nabla_x \Delta_x Q_j = \\ &\frac{\epsilon}{\Delta x} (Q_{j+3} - 6Q_{j+2} + 15Q_{j+1} - 20Q_j + 15Q_{j-1} - 6Q_{j-2} + Q_{j-3}) \equiv \epsilon(\Delta x)^5 \partial_{xxxxxx} Q_j \end{aligned}$$

a 5^{th} order accurate term representing a 6^{th} derivative, requiring three fringe points.

The generalized form of artificial dissipation shown in Eq. 8, uses a mixture of 2^{nd} , 4^{th} and 6^{th} derivative artificial dissipation, employing a pressure gradient switch and spectral radius scaling. Note that the stencil widths and fringe points requirements are consistent with up to a 6^{th} order accurate flux difference operator. Typical values of the constants are $\epsilon_2 \approx 1$ (for use in flows with shock waves), $\epsilon_4 \approx 0.01$ for 3^{rd} order accuracy (if $\epsilon_6 = 0$) and $\epsilon_6 = 0.001$ for 5^{th} order accuracy (if $\epsilon_4 = 0$).

The combination of central flux finite differences of various orders with the various choices of order and artificial dissipation type result in accuracy order options in OVERFLOW (for convenience of discussion the OVERFLOW input parameter variable FSO is used to designate the order of accuracy options)

- FSO=2 Uses 2^{nd} order flux difference Eq. 5 and 3^{rd} order artificial dissipation, $\epsilon_4 \neq 0, \epsilon_6 = 0$. Fringe stencil requirement 2.
- FSO=3 Uses 4^{th} order flux difference Eq. 6 and 3^{rd} order artificial dissipation, $\epsilon_4 \neq 0, \epsilon_6 = 0$. Fringe stencil requirement 2.
- FSO=4 Uses 4^{th} order flux difference Eq. 6 and 5^{th} order artificial dissipation, $\epsilon_4 = 0, \epsilon_6 \neq 0$. Fringe stencil requirement 3.
- FSO=5 Uses 6^{th} order flux difference Eq. 7 and 5^{th} order artificial dissipation, $\epsilon_4 = 0, \epsilon_6 \neq 0$. Fringe stencil requirement 3.

In practice, FSO=5, the 6^{th} order central difference scheme, Eq. 7, coupled with 5^{th} order artificial dissipation, Eq. 8, has been quite effective for many applications of interested, e.g., resolving vortex flows and rotor-craft wakes. Dissipation coefficients of $\epsilon_2 = 0.0$, $\epsilon_4 = 0.0$ and $\epsilon_6 = 0.001$ are typical. As shown below, this scheme does a good job in minimizing both vortex dissipation and dispersion error, relative to the 2^{nd} order difference scheme with 3^{rd} order dissipation, but its cost is only about 10% more work. It does require 3 fringe cells rather than 2, which means a larger volume of data is exchanged at inter-block boundaries, but in general tests have shown the improved accuracy outweighs this relatively minor extra communication cost.

III.C. Vortex Propagation Results with Central Finite Differences and Artificial Dissipation

There are two types of error of concern, propagation error (sometimes described as dispersion error or convective error) and amplitude error (dissipation error, diffusion error). For the vortex propagation example problem, the convective error is directly a product of the choice of flux differences and the dissipation error comes from the artificial dissipation. The choice of the time advance scheme also introduces convective and dissipation error, but will not be discussed further here. For all the results presented in this section, a time step and time advance scheme was chosen which reduces the temporal error below the spatial finite difference errors.

Figure 2a shows a centerline cut (across the vortex core y location) of density compared with the exact solution after 60 C_d demonstrating typical convective error and dissipation error. Figure 2b shows density contours, where the black contours are the exact solution and the colored contours are the computed solution after 3 passes of the vortex through the domain. The vortex core has decayed due to the level of artificial dissipation and the location of the core is compromised by the convective errors.

The decay of the vortex core is directly related to the level of artificial dissipation. Reducing the coefficient of the artificial dissipation will reduce the core decay, but at the expense of robustness, stability, and increased oscillations (non-smoothness or the generation of high frequency error). Figure 3 shows a comparison using the 4^{th} order central difference scheme for the fluxes on a 20 grid point after 10 C_d, using $\epsilon_4 = 0.01$ and $\epsilon_4 = 0.001$. Now the level of artificial dissipation can be controlled by ϵ and the behavior as $\Delta x \to 0$ is 3^{rd} order, but the actual form of the error is a 4^{th} derivative, $\partial_{xxxx} Q_j$. The lower artificial dissipation leads to high frequency oscillations and eventually that case diverges. An analysis can be found in Pulliam[12] of artificial dissipation schemes for both stability and robustness within the framework of an implicit flow solver, e.g. OVERFLOW.

Figures 4a,b shows the result of integration using 2^{nd} order central differences for the fluxes and 3^{rd} order artificial dissipation (FSO=2) with $\epsilon_2 = \epsilon_6 = 0$ and $\epsilon_4 = 0.04$ (a more typically value used in OVERFLOW) which has an overall 2^{nd} order accuracy. The main effect of the flux differencing choice on the vortex is dispersion error resulting in a displacement of the vortex core. A line cut across the vortex centerline is

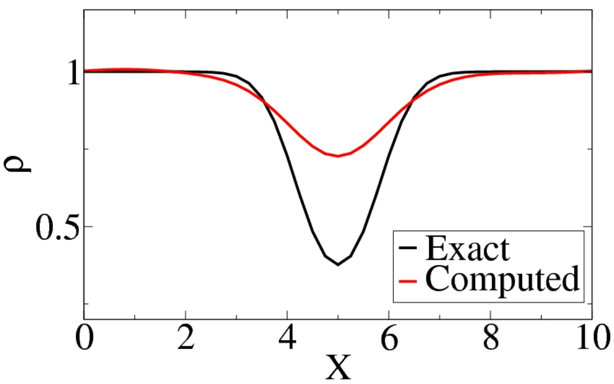

(a) Centerline Density

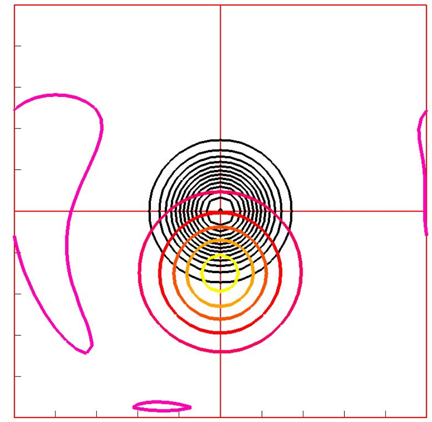

(b) Density Contours

Figure 2. Convective Error Example: 60 C_d, $FSO = 2$, $\epsilon_4 = 0.01$

shown in Fig. 4a comparing the exact and computed solutions. The computed vortex has decayed, mainly due to the artificial dissipation. The computed vortex core is displaced due to the dispersion error of the finite difference operator, note the core location off the centerline in Fig. 4b. Figures 4c,d shows the result of integration using 4^{th} order central differences and the 3^{rd} order artificial dissipation, (FSO=3, $\epsilon_2 = \epsilon_6 = 0$ and $\epsilon_4 = 0.04$). Again the computed vortex has decayed (mainly due to the artificial dissipation), but the displacement evident in the 2^{nd} order results is reduced, as a result of the more accurate convection properties of the 4^{th} order scheme. Figure 4e,f shows the result of integration using 6^{th} order central differences and 5^{th} order artificial dissipation, (FSO=5, $\epsilon_2 = \epsilon_4 = 0$ and $\epsilon_6 = 0.001$). The dispersion and dissipation errors are greatly reduced and now the vortex more accurately tracks the centerline and strength.

III.D. 3^{rd} Order HLLC and 5^{th} Order WENO Schemes

Nichols, Tramel, and Buning.[11] presented the development, implementation and assessment of a 3^{rd} order HLLC scheme and 5^{th} order WENO scheme and variants of those methods, including the various limiters employed. Details of the implementation in OVERFLOW can be found in that reference and will not be repeated here. Results from the 3^{rd} order HLLC and 5^{th} order WENO scheme for $30C_d$ are shown in Fig. 5. The 3^{rd} order HLLC schemes is as dissipative as the 3^{rd} order central scheme, FSO=3, while the 5^{th} order WENO scheme is consistent with the 5^{th} order central method, FSO=5.

IV. Boundary Conditions, Domain Connectivity, Parallelization Splittings

The implementation of higher order wider stencil finite difference operators requires careful considerations, especially in the boundary regions of the OVERFLOW process. There are a number of boundary conditions/operators to consider. The physical boundaries, such as walls, inflow/outflow, symmetries and periodicity, are handled appropriately in OVERFLOW and stencils for difference operators are applied which respect the boundary type. OVERFLOW uses the overset approach to domain decomposition to handle the topology of geometries and for parallelization. There are two types of domain connectivity boundaries found in OVERFLOW. The initial overset grids are interfaced either with predetermined Pegasus[2] connectivity or through the internally generated Domain Connectivity Framework (DCF)[5] and X-rays. In both cases, appropriate fringe points are added so that boundaries stencils for the finite differences are not degraded. In addition to the overset grid systems decomposition, the initial grids may be split to achieve parallel load balancing. Based on the number of processors (cores, threads) a domain splitting occurs which may break each initial grid multiple times until a larger number of grids below a target grid size are produced. This new system of grids is then packed onto the processors to produce a better load balance of work for good parallel efficiency. In the splitting process, (appropriate for the chosen difference scheme) additional fringe points

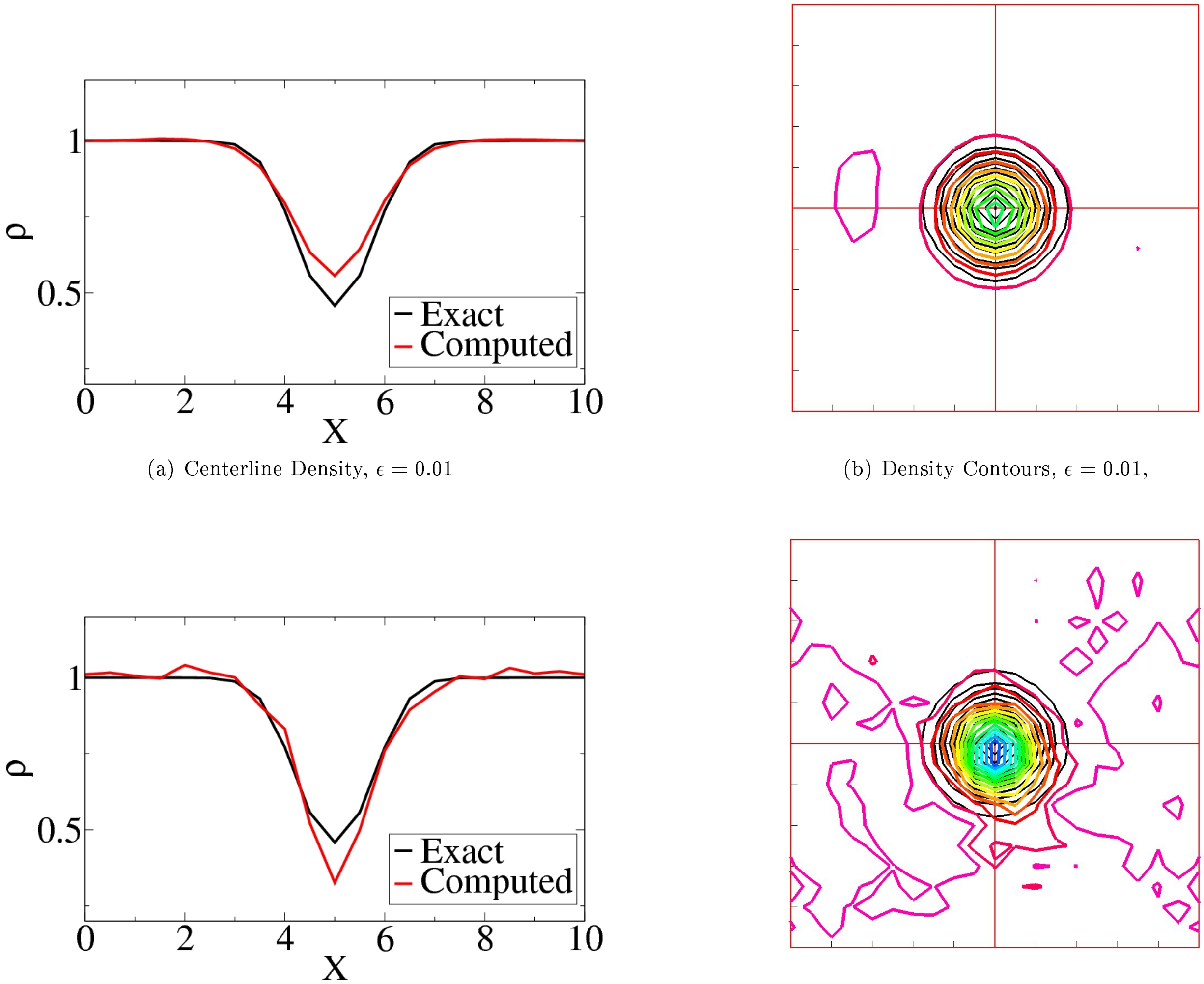

(a) Centerline Density, $\epsilon = 0.01$

(b) Density Contours, $\epsilon = 0.01$,

(c) Centerline Density, $\epsilon = 0.001$

(d) Density Contours, $\epsilon = 0.001$

Figure 3. Dissipation Error Example : 10 C_d.

are added at each split boundary to provide an interface with point to point injection domain connectivity. This process of adding fringe points does produce a slight overhead in terms of memory, but it makes the implementation of the higher order operators seamless at the split boundaries.

In places where either a physical boundary requires a smaller stencil size (at a solid wall the next point above the surface is an interior point without fringe support above 1) or the domain connectivity fails to produce multiple fringe points, the difference stencils are reduced appropriately in order as the boundary is approached. For example, assuming indexing $j = 1, 2, 3, 4, \cdots$, if the 6^{th} order central flux difference, Eq. 7, is used for interior points $j \geq 4$, then at $j = 3$ the 4^{th} order central difference, Eq. 6 is used and at $j = 2$, the 2^{nd} order central difference, Eq. 5 is applied. The artificial dissipation operators are handled in similar fashion, as are the other methods, 3^{rd} order HLLC and 5^{th} order WENO, see Nichols,et al.[11]

V. Implication of High Order Operators to Implicit Time Advance Methods

OVERFLOW employs an implicit approximate factorization[13,14] scheme for the time integration. This requires both the linearization of the flux derivative terms, artificial dissipation operators, and viscous terms, as well as the solution of the implicit operators which are either block tridiagonal matrices in each coordinate direction or scalar pentadiagonal operators in the diagonalized approach of Pulliam and Chaussee.[15] It is a common practice to reduce the order of accuracy of the space derivative terms in the implicit operators

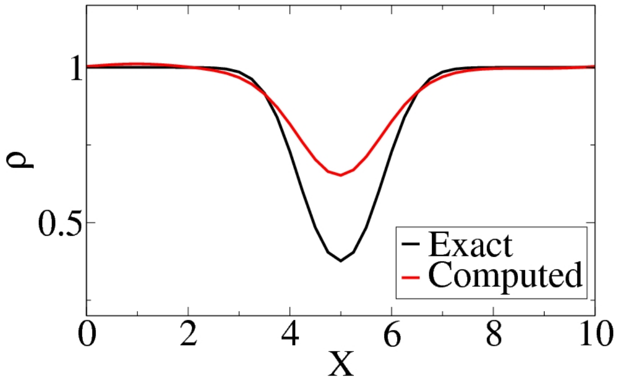

(a) Centerline Density, FSO=2, 2^{nd} Order

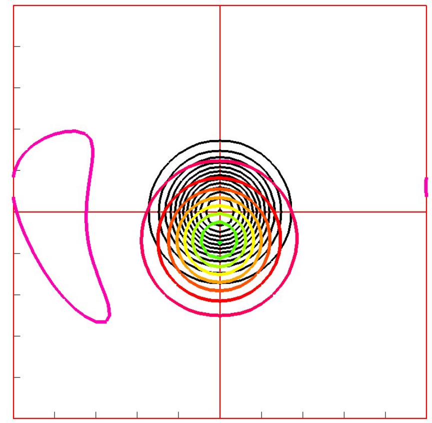

(b) Density Contours, FSO=2, 2^{nd} Order

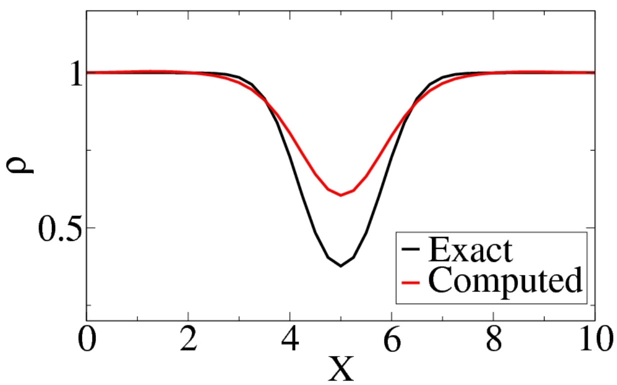

(c) Centerline Density, FSO=3, 3^{rd} Order

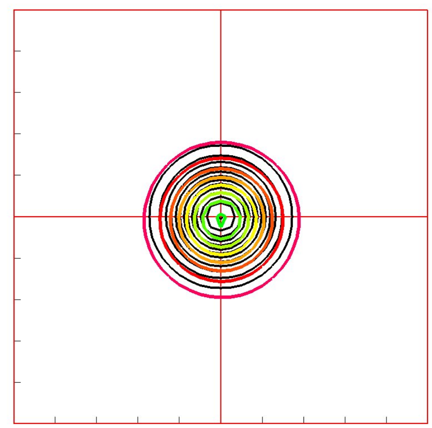

(d) Density Contours, FSO=3, 3^{rd} Order

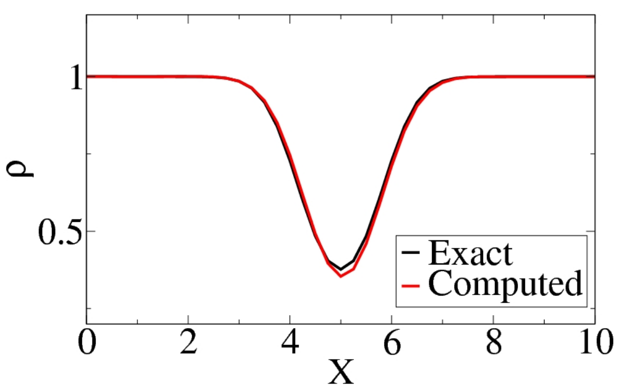

(e) Centerline Density, FSO=5, 5^{th} Order

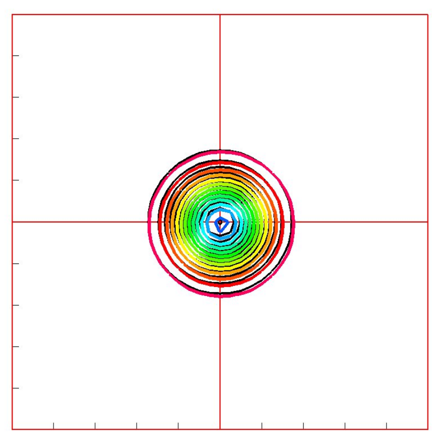

(f) Density Contours, FSO=5, 5^{th} Order

Figure 4. Computed Vortex: 30 C_d.

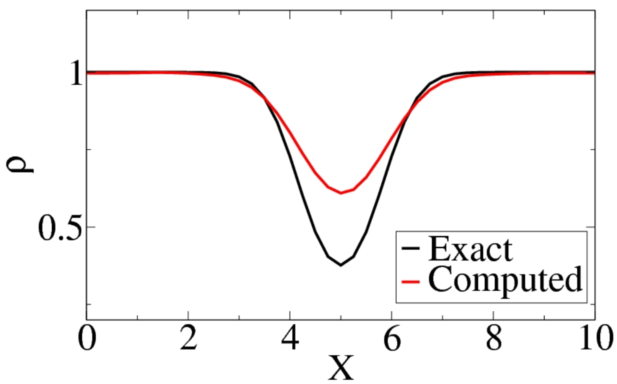

(a) Centerline Density, 3^{rd} Order HLLC

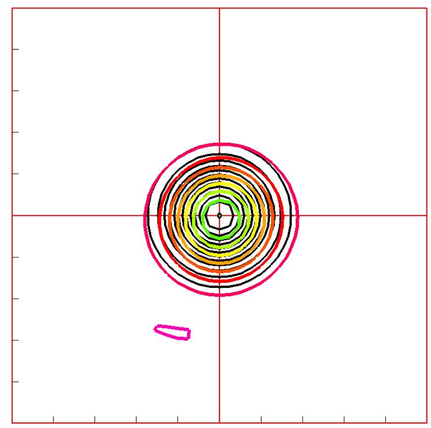

(b) Density Contours, 3^{rd} Order HLLC

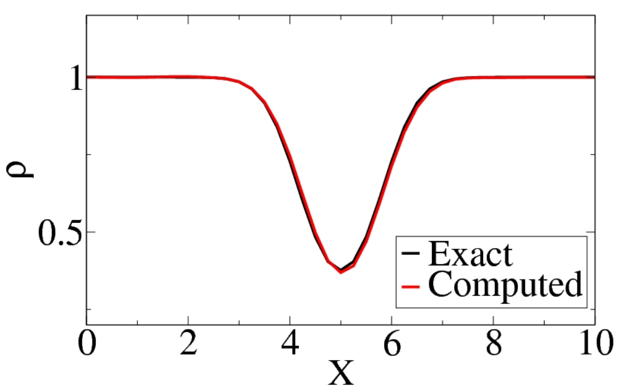

(c) Centerline Density, 5^{th} Order WENO

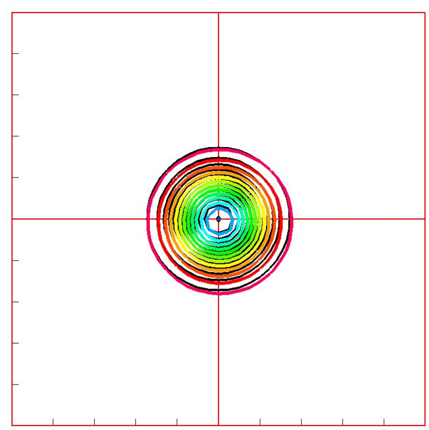

(d) Density Contours, 5^{th} Order WENO

Figure 5. Computed Vortex: 30 C_d.

to control the band width of the matrices and therefore reduce the computational expense. For example, OVERFLOW also has an hybrid SSOR time advance algorithm based on a 1^{st} order accurate form of Steger-Warming flux splitting,[16] usually used with the 3^{rd} order HLLC or 5^{th} order WENO schemes.[11] Depending on the implicit operator band width, 3 for block tridiagonal and 5 for scalar pentadiagonal, the flux derivative operator in the implicit matrix can only support either a 3 point stencil or a 5 point difference stencil. Therefore, in the block tridiagonal option a 2^{nd} order difference is used for the flux derivatives, Eq. 5, even though a higher order operator may be used for the right-hand-side (residual) flux derivatives, for example, Eq. 7. Similarly, for the diagonalized scalar pentadiagonal scheme, a 4^{th} order difference, Eq. 6, is used for the implicit operator in combination with a residual flux derivatives of 4^{th} order or higher. Linear analysis[14,17] shows that these options are stable.

The artificial dissipation, Eq. 8, is subject to similar restrictions on the implicit operator side. The implicit linearization of the artificial dissipation is discussed in Pulliam.[12] OVERFLOW uses a reduced operator approach where for the block tridiagonal scheme, a 1^{st} order 3 point stencil dissipation operator is used in the implicit implementation, effectively, $\Upsilon = 1, \epsilon_2 \neq 0, \epsilon_4 = 0, \epsilon_6 = 0$, in Eq. 8. In the scalar pentadiagonal option, the linearized artificial dissipation operator can be extended to 5 points, the reduced form is effectively equivalent to Eq. 8 with $\Upsilon = 1, \epsilon_2 = 0, \epsilon_4 \neq 0$ and $\epsilon_6 = 0$. Linear analysis[12] shows that the coefficients for the implicit linearized artificial dissipation needs to be at least 2 times the coefficients used on the flux terms in the residual and in fact the conservative choice in OVERFLOW is a factor of 4.

VI. Viscous Terms and Metrics

The viscous terms in OVERFLOW are differenced to 2^{nd} order, including the cross terms. Even though higher order treatment of the viscous terms is possible, (cross terms may be complicated), the improved accuracy may not be justifiable or measurable. For realistic geometries, the viscous effects are usually restricted to the boundary layer regions where wall normal spacing is small compared to the other coordinate directions. Second order accuracy should be sufficient in the wall normal regions and viscous terms negligible in the other directions. Even in the case of DES[18] or LES[19] computations where homogeneous turbulence concepts dominate, it is not clear whether higher order accurate viscous treatment will pay dividends (in DES for example, the grid requirements are dictated more by eddy resolution concepts than by simple accuracy considerations).

The metric (generalized coordinates) terms are computed to 2^{nd} order accuracy in OVERFLOW. In the OVERFLOW-D mode off-body grids are uniform Cartesian and therefore, the metrics are constant and will not affect accuracy. For generalized curvilinear grids, the use of 2^{nd} order metrics means that the formal accuracy is 2^{nd} order, even when higher order differences are used for the fluxes. In general though, grids are assumed to be smoothly varying, have adequate resolution in appropriate regions and so even though the formal accuracy would be 2^{nd} order due to the metrics, the increased flux difference accuracy will be effective.

Obviously, other approximations and simplifications (e.g., boundary conditions, domain connectivity and interpolations) affect the overall formal accuracy of OVERFLOW. In fact, it would be incorrect to classify OVERFLOW with the recent improvement, as a high order accurate code. The higher order flux differences and reduced artificial dissipation which can be used with up to 5^{th} order accuracy do improve the overall accuracy of the computations without degrading the robustness, stability, or convergence.

VII. Complex Flow Results

A large selection of application examples in two and three dimensions have been computed using the 5^{th} order scheme described above.[20,21] A representative result is given here for the Tilt Rotor Aeroacoustics Model (TRAM), a 1/4-scale three blades and hub component of the V-22 Osprey tiltrotor aircraft.[22,23] Extensive details of the physical problem, geometry, experimental data and previous numerical studies can be found in Potsdam and Strawn.[24] The goal is to compute the steady hover mode of the TRAM blade system. Therefore, the OVERFLOW computations were performed in a steady non-inertial frame where the observer is moving with the blades and the flow appears stationary with respect to the observer. The one-equation Baldwin-Barth turbulence model was used with corrections, Potsdam and Pulliam.[25]

The three-bladed TRAM rotor system is shown in Figure 6, along with a coordinate slice showing the near body curvilinear and off body grid system. In terms of the structured overset methodology employed by

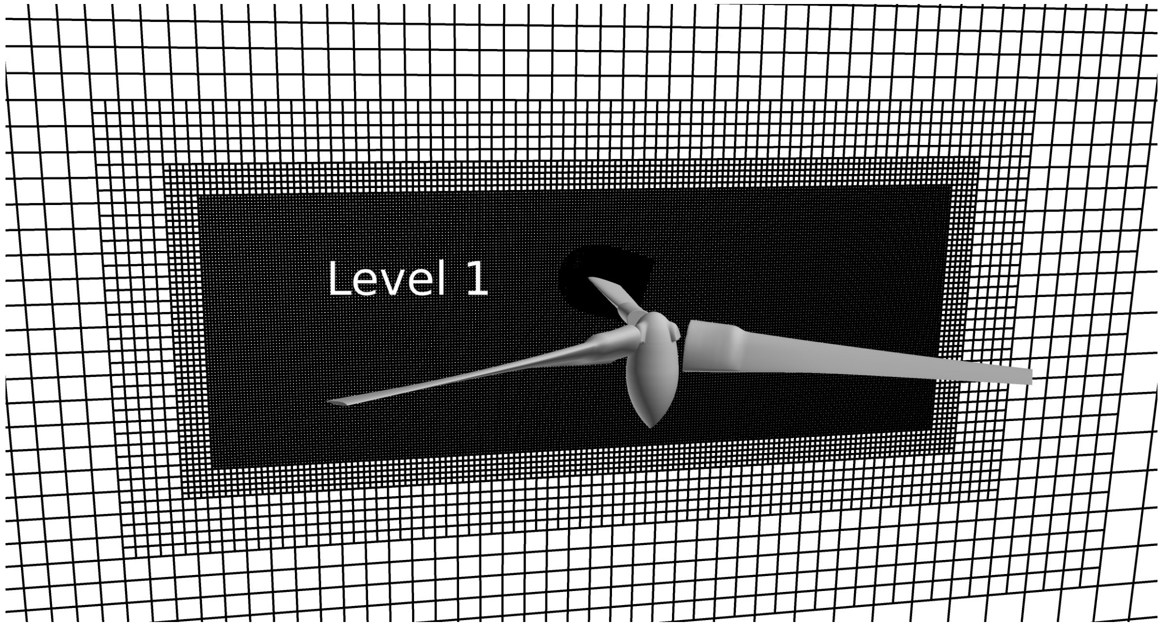

Figure 6. TRAM V22 geometry, Hover

Case	ΔL_1	No. of grid points	No. of grids
Small	$0.1 \cdot C_{\text{tip}}$	13,692,987	50
Medium	$0.05 \cdot C_{\text{tip}}$	58,426,144	70
Large	$0.025 \cdot C_{\text{tip}}$	379,761,734	188
Huge	$0.0125 \cdot C_{\text{tip}}$	3,087,812,624	194

Table 1. Grid Size for Different Refinement Levels

OVERFLOW, near-body (NB) curvilinear structured grids are generated about the blade and hub geometries with sufficient resolution to capture viscous effects. The reference length scale for this problem is the tip chord (C_{tip}) of the blades. Off body Cartesian grids are automatically generated by OVERFLOW. The "Baseline" case as defined in Potsdam and Strawn uses a Level 1 grid (L_1), which is uniform in all coordinate directions with a grid spacing $\Delta L_1 = 0.1 C_{\text{tip}}$. The near body grids are completely embedded within the L_1 grid, where the overset methodologies of hole cutting, blanking, and Chimera interpolation logic are employed to interface the grid systems.[3,5] Subsequent off body Level 2 (L_2) and higher Cartesian brick grids are generated with spacing $\Delta L_i = 2^{i-1} \Delta L_1$ to extend the grid to the outer boundary of the computational domain, see Figure 6.

The Baseline grid of Potsdam and Strawn is a standard for comparison and will be used for the comparisons here. Table 1 lists the characteristics of the Baseline grid and a sequence of uniform off body grid refinements. These grids are a sequence of halvings of the L_1 spacing to improve the resolution of the wake vortices being shed off the blade tips. The "Huge" mesh for example represents three levels of refinement of the L_1 spacing and produces a grid with over 3 billion points, possibly the largest aerodynamic RANS CFD calculation to date.[26]

Shown in Fig. 7 is a comparison of the solution on the Baseline grid system (referred to as "Small" grid) with the solution on the Medium grid system at the two accuracy choices, 3^{rd} and 5^{th} order. The results of the Baseline case are exactly consistent with those reported by Potsdam and Strawn[24] and Potsdam and Pulliam.[25] On the same grid, e.g. the small grid, the increased resolution and decreased error of the 5^{th} order scheme allows the tip vortices to persist longer. On the medium grid, the displacement of the vortex due to increased dispersion error at the lower accuracy is evident. In Fig. 7, iso-surfaces of vorticity show that the refined grid captures the wake vortex more accurately than the Baseline grid, producing significantly less decay of the vortex cores. Figure 8 shows vorticity contours at the $y = 0$ plane cut from the Baseline

(Small), Medium grid, and Large grid for 3^{rd} order accuracy, (FSO=3), and 5^{th} order accuracy, (FSO=5). Both grid refinement and increased order of accuracy improve the tip vortex capturing and quality of the vortex cores. Also note that increased resolution and accuracy improve the capturing of the blade trailing edge wakes and their subsequent interaction with the tip vortices.

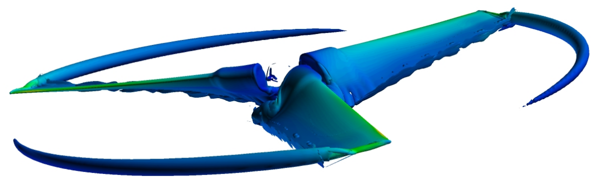

(a) Small grid, 3^{rd} Order

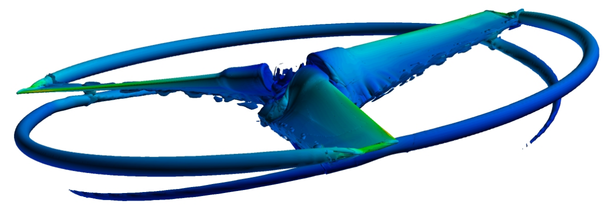

(b) Small grid, 5^{th} Order

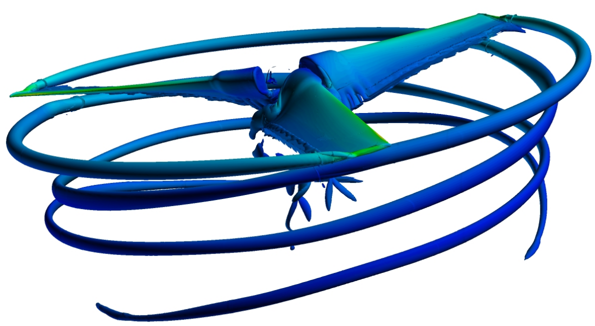

(c) Medium grid, 3^{rd} Order

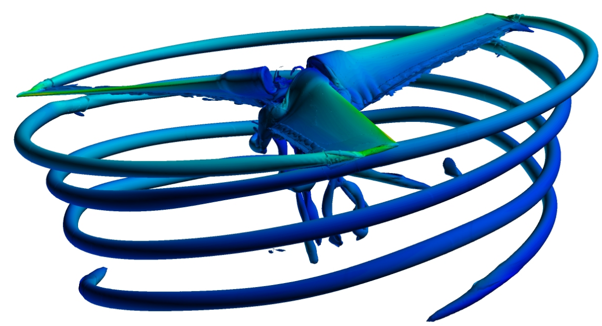

(d) Medium grid, 5^{th} Order

Figure 7. Iso-Surface Results for Small and Medium Grid, 3^{rd} and 5^{th} Order Accuracy

One measure of the effect of increased resolution and accuracy on the capturing of rotor wake vortices is the growth rate of the vortex cores as a function of azimuthal angle measured from one of the blade tips. The vortex core diameter as the distance between the minimum and maximum cross-flow velocity components (normalized by blade tip chord). Then the growth of the vortex core as a function of wake age (azimuthal angle) can be constructed using the velocity profiles and is displayed in Fig 9. Also shown is a composite of experimental data, from Holst and Pulliam.[27] The results of a grid refinement sequence demonstrate marked improvement of the rate of decay of the vortex core. This culminates in the Huge grid with 5^{th} order accuracy giving a rate comparable to the experimental data.

VIII. Summary

Higher order accurate central finite difference options in OVERFLOW have been presented and demonstrate the accuracy improvements for practical complex flows. The methods fit well in the overset structure of OVERFLOW and do not hamper the parallel efficiency of the code. The approach provides a simple (both in implementation and concept) method for improving the solution accuracy.

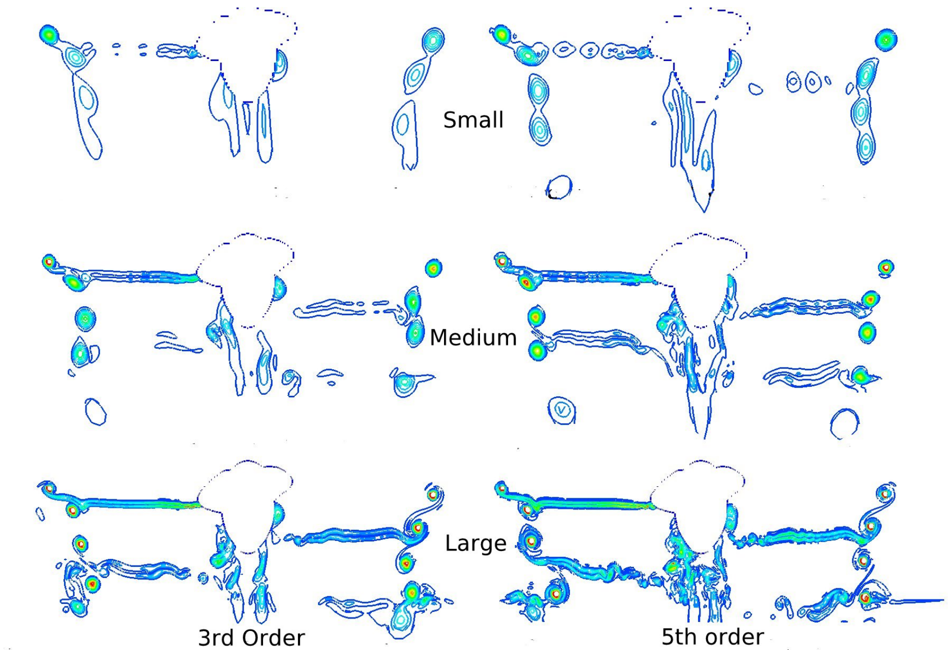

Figure 8. **Vorticity Contours at $y = 0$ Cross-section Comparing 3^{rd} and 5^{th} Order Accuracy**

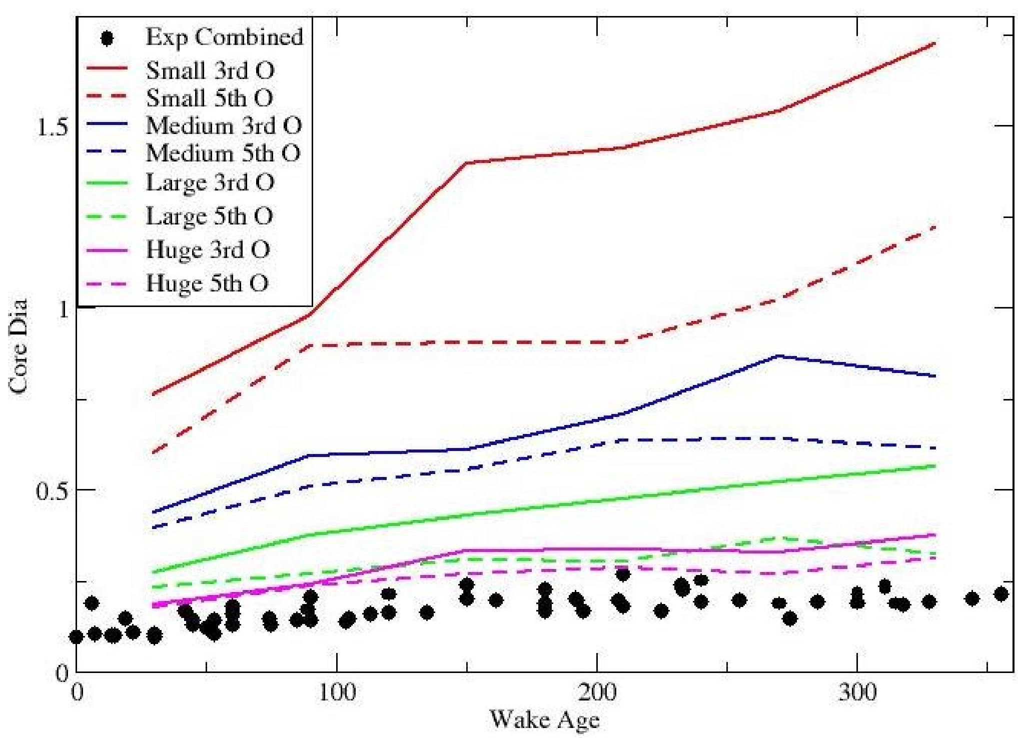

Figure 9. **Growth Rate of Vortex Core with Wake Age**

References

[1]OVERFLOW: http://aaac.larc.nasa.gov/ buning/codes.html#overflow

[2]Rogers, S. E., Suhs, N. E., and Dietz, W. E., "PEGASUS 5: An Automated Pre-processor for Overset-Grid CFD," AIAA Journal, Vol. 41, No. 6, 2003, pp. 1037-1045.

[3]Meakin, R.L. 2001. "Automatic Off-body Grid Generation for Domains of Arbitrary Size," *AIAA 15th Computational Fluid Dynamics Conference*, Anaheim, CA, paper no. AIAA-2001-2536.

[4]Meakin, R.L., "Object X-Rays for Cutting Holes in Composite Overset Structured Meshes", AIAA-2001-2537, June 2001

[5]Chan, W.M. 2009. "Overset Grid Technology Development at NASA Ames Research Center." *Computers and Fluids*, 38(3):496-503.

[6]Nichols, R.H., Tramel, R.W., Buning, P.G. "Users Manual for OVERFLOW 2.1, Version 2.1t Aug 2008"

[7]Benek, J.A., Buning, P.G., Steger, J.L. 1985. "A 3-D Chimera Grid Embedding Technique," *AIAA 7th Computational Fluid Dynamics Conference*, Cincinnati, OH, AIAA-85-1523.

[8]Buning, P.G., Chiu, I.T., Obayashi, S., Rizk, Y.M., Steger, J.L. 1988. "Numerical Simulation of the Integrated Space Shuttle Vehicle in Ascent," *AIAA Atmospheric Flight Mechanics Conference*, Minneapolis, MN, AIAA-1988-4359.

[9]Jespersen, D.C., Pulliam, T.H., Buning, P. G., "Recent enhancemnts to OVERFLOW," AIAA Paper 97-0644, Jan. 1997.

[10]Nichols, R.H., Tramel, R.W., Buning, P.G., "Solver and Turbulence Model Upgrades to OVERFLOW 2 for Unsteady and High-Speed Applications," AIAA Paper 2006-2824, 24th AIAA Applied Aerodynamics Conference, San Francisco, CA, June 2006.

[11]Nichols, R.H., Tramel, R.W., Buning, P.G., "Evaluation of Two High Order WENO Schemes," AIAA Paper 2007-3920, 25th AIAA Applied Aerodynamics Conference, Miami, FL, June 2007.

[12]Pulliam, T.H., "Artificial Dissipation Models for the Euler Equations", AIAA J., Vol 24, No 12 p. 1931, 1986.

[13]Beam, R. and Warming, R. F., "An Implicit Finite-Difference Algorithm for Hyperbolic Systems in Conservation Law Form," J. Comp. Phys., Vol. 22, 1976, pp. 87-110.

[14]Pulliam, T.H., "Efficient Solution Methods for the Navier-Stokes Equations," Lecture Notes for the von Kármán Institute For Fluid Dynamics Lecture Series: Numerical Techniques for Viscous Flow Computation In Turbomachinery Bladings, von Kármán Institute, Rhode-St-Genese, Belgium, 1985.

[15]Pulliam, T. H. and Chaussee, D. S., "A Diagonal Form of an Implicit Approximate Factorization Algorithm," J. Comp. Phys.,Vol. 39, p. 347, 1981.

[16]Steger, J. L. and Warming, R. F., "Flux Vector Splitting of the Inviscid Gas Dynamic Equations with Applications to Finite Difference Methods," J. Comp. Phys., Vol. 40, pp. 263-293, 1981.

[17]Pulliam, T. H. and Steger J. L., "On Implicit Finite-Difference Simulations of Three-Dimensional Flow," AIAA Journal Vol. 18, 1980 p. 159.

[18]Spalart, P. R., Deck, S., Sur, M. L., Squires, K. D., Strelets, M. and Travin, A., "New Version of Detached-Eddy Simulation, Resistant to Ambiguous Grid Densities", Theoretical and Computational Fluid Dynamics (2006), Vol. 20, No. 3, pp. 181-195.

[19]Spalart, P., Jou, W-H., Strelets, M., and Allmaras, S. "Comments on the Feasibility of LES for Wings and on a Hybrid RANS/LES Approach", First AFOSR Conference on DNS/LES, August 1997, Greyden Press, Columbus, OH.

[20]Ahmad, J. U., Chaderjian, N.M., "High-Order Accurate CFD/CSD Simulation of the UH60 Rotor in Forward Flight", 29th AIAA Applied Aerodynamcis Conference, (submitted for publication), Honolulu, Hawaii, June 2011

[21]Chaderjian, N.M., Buning, P. G. "High Resolution Navier-Stokes Simulation of Rotor Wakes", Presented at AHS 67th Annual Forum and Technology Display, Virginia Beach, Va, May 2011.

[22]Swanson, S. M., McCluer, M. S., Yamauchi, G. K., and Swanson, A. A., "Airloads Measurements from a 1/4-Scale Tiltrotor Wind Tunnel Test", 25th European Rotorcraft Forum, Rome, Italy, September 1999.

[23]Johnson, J. L., and Young, L. A., "Tilt Rotor Aeroacoustic Model Project", Confederation of European Aerospace Societies (CEAS), Forum on Aeroacoustics of Rotorcraft and Propellers, Rome, Italy, June 1999.

[24]Potsdam, M. A. Strawn, R. C. 2005. "CFD Simulations of Tiltrotor Configurations in Hover," *Journal of the American Helicopter Society*, 50(1):82-94.

[25]Potsdam, M. A., Pulliam, T. H. 2008. "Turbulence Modeling Treatment for Rotocraft Wakes," presented at the AHS Aeromechanics Specialist's Meeting, San Francisco, CA, January 23-25, 2008.

[26]Pulliam,T.H., Jespersen, D.C., "Large Scale Aerodynamic Calculation on Pleiades", International Conference on Parallel Computational Fluid Dynamics, Moffett Field, Ca, May 18-22, 2009.

[27]Holst, T.L., Pulliam, T.H. 2009. "Overset Solution Adaptive Grid Approach Applied to Hovering Rotorcraft Flows," *AIAA 27th Applied Aerodynamics Conference, San Antonio, Texas*, Paper No. AIAA-2009-3519.